Influence of the Bi^{3+} electron lone pair in the evolution of the crystal and magnetic structure of $La_{1-x}Bi_xMn_2O_5$ oxides

2013 J. Phys.: Condens. Matter 25 216002

(http://iopscience.iop.org/0953-8984/25/21/216002)

J. Phys.: Condens. Matter **25** (2013) 216002 (11pp) doi:10.1088/0953-8984/25/21/216002

Influence of the Bi^{3+} electron lone pair in the evolution of the crystal and magnetic structure of $La_{1-x}Bi_xMn_2O_5$ oxides

M Retuerto[1], A Muñoz[2], M J Martínez-Lope[3], M Garcia-Hernandez[3], G André[4], K Krezhov[5] and J A Alonso[3]

[1] Department of Chemistry, Rutgers State University of New Jersey, Piscataway, NJ 08854-8087, USA
[2] Departamento de Física Aplicada, EPS, Universidad Carlos III, Avenida Universidad 30, E-28911 Leganés-Madrid, Spain
[3] Instituto de Ciencia de Materiales de Madrid, C.S.I.C., Cantoblanco E-28049 Madrid, Spain
[4] Laboratoire Leon Brillouin, CEA/Saclay, F-91191 Gif Sur Ivette Cedex, France
[5] Institute for Nuclear Research and Nuclear Energy, Bulgarian Academy of Sciences, 72 Tsarigradsko Chaussee Boulevard, Sofia, 1784, Bulgaria

E-mail: retuerto@rci.rutgers.edu

Received 8 March 2012, in final form 11 July 2012
Published 30 April 2013
Online at stacks.iop.org/JPhysCM/25/216002

Abstract

$La_{1-x}Bi_xMn_2O_5$ ($x = 0$, 0.2, 0.4, 0.6, 0.8 and 1) oxides are members of the RMn_2O_5 family. The entire series has been prepared in polycrystalline form by a citrate technique. The evolution of their magnetic and crystallographic structures has been investigated by neutron powder diffraction (NPD) and magnetization measurements. All the samples crystallize in an orthorhombic structure with space group *Pbam* containing infinite chains of $Mn^{4+}O_6$ octahedra sharing edges, linked together by $Mn^{3+}O_5$ pyramids and (La/Bi)O_8 units. These units become strongly distorted as the amount of Bi increases, due to the electron lone pair of Bi^{3+}. All the members of the series are magnetically ordered below $T_N = 25$–40 K and they present different magnetic structures. For the samples with low Bi content ($x = 0.2$ and 0.4) the magnetic structure is characterized by the propagation vector $\mathbf{k} = (0, 0, 1/2)$. The magnetic moments of the Mn^{4+} ions placed at octahedral sites are ordered according to the basis vectors (G_x, A_y, 0) whereas the Mn^{3+} moments, located at pyramidal sites, are ordered according to the basis vectors (0, 0, C_z). When the content of Bi increases, two different propagation vectors are needed to explain the magnetic structure: $\mathbf{k}_1 = (0, 0, 1/2)$ and $\mathbf{k}_2 = (1/2, 0, 1/2)$. For $x = 0.6$ and 0.8, $\mathbf{k}_2$ is predominant over $\mathbf{k}_1$ and for this propagation vector ($\mathbf{k}_2$) the magnetic arrangement is defined by the basis vectors (G_x, A_y,0) and (F_x, C_y, 0) for Mn^{4+} and Mn^{3+} ions, respectively.

(Some figures may appear in colour only in the online journal)

1. Introduction

In recent years much research has focused on the materials known as magnetoelectrics, in which magnetism and ferroelectricity coexist and are mutually coupled [1, 2]. These materials display phenomena such as the control of the electrical polarization by the application of an external magnetic field. This behavior has recently been found in some compounds of the family of oxides with the formula RMn_2O_5 [3]. RMn_2O_5 oxides crystallize in an orthorhombic structure with space group *Pbam*, where the manganese ions occupy two different crystallographic positions with distinct oxygen coordination and oxidation states [4, 5]. Mn^{4+} cations are octahedrally coordinated to oxygen (4f sites), whereas Mn^{3+} cations are bonded to five oxygen atoms, forming distorted tetragonal pyramids (4h sites).

Very recently, it has been reported in some members of the RMn_2O_5 family of compounds that the magnetic transition coincides with an anomaly in the dielectric constant [6–10]. Therefore, it is of paramount importance to study the magnetic structures of these oxides in order to establish whether or not the loss of symmetry induced by the magnetic structure is the origin of the anomalies observed in the permittivity curves. RMn_2O_5 oxides present antiferromagnetic ordering, with different magnetic structures depending on the R cation. $LaMn_2O_5$ presents a long-range magnetic ordering characterized by a commensurate magnetic structure with a propagation vector $\mathbf{k} = (0, 0, 1/2)$ and $T_N \sim 35$ K [11]. The magnetic arrangement is defined by the basis vectors $(G_x, A_y, 0)$ and $(0, 0, C_z)$ for the Mn^{4+} and Mn^{3+} ions, respectively. At 3.5 K, the magnetic moments are 2.59(4) and 1.61(7) μ_B for the Mn^{3+} (4h site) and Mn^{4+} ions (4f site), respectively, and the magnetic moments are directed along the *c* axis for Mn^{4+} moments and lie in the *ab* plane for Mn^{3+} moments [11]. $BiMn_2O_5$ also presents a commensurate magnetic structure, becoming magnetically ordered below $T_N \sim 39$ K, and its magnetic structure is defined by the propagation vector $\mathbf{k} = (1/2, 0, 1/2)$. For the Mn^{3+} ions the magnetic moments are ordered according to the basis vectors $(F_x, C_y, 0)$ and for the Mn^{4+} ions the basis vectors are $(G'_x, A'_y, 0)$. At $T = 1.6$ K, the magnetic moments for Mn^{3+} and Mn^{4+} cations are 3.23(6) μ_B and 2.51(7) μ_B, respectively, and all the magnetic moments lie in the *ab* plane [12, 13]. Vecchini *et al* [14] have found a small difference in the magnetic structure of $BiMn_2O_5$ in single crystals compared to Muñoz *et al* in polycrystalline samples [13]. They have found antiferromagnetic (–Mn^{4+}–Mn^{3+}–Mn^{3+}–Mn^{4+}–) chains in the *ab* plane. This completes the description given by Muñoz *et al*, as a non-collinear arrangement of Mn^{4+} and Mn^{3+} moments within one AFM chain.

Nevertheless, the rest of the RMn_2O_5 oxides described so far (R = Nd, Tb, Ho, Er, Y and Eu) show incommensurate magnetic structures defined by the propagation vector $\mathbf{k} = (1/2, 0, \tau)$, where the Mn spins are ordered according to a helicoidal structure with the magnetic moments lying in the *ab* plane [15–17]. A more detailed study of R = Er, Tb revealed that the amplitude of the Mn moments is modulated. Finally, the magnetic structure of $DyMn_2O_5$ was defined by two different propagation vectors $\mathbf{k}_1 = (1/2, 0, 0)$ and $\mathbf{k}_2 = (1/2, 0, \tau)$ [18]. When R^{3+} is a magnetic rare earth, it orders magnetically at low temperatures with sinusoidal magnetic structures.

In the present work we study the series $La_{1-x}Bi_xMn_2O_5$ ($x = 0$, 0.2, 0.4, 0.6, 0.8, 1) to assess the evolution of the crystal structure, magnetism and magnetic structure when La is substituted by Bi. We compare the magnetic structures across the series with those of the parent compounds $LaMn_2O_5$ and $BiMn_2O_5$ from powder diffraction data and magnetization measurements.

2. Experimental details

The oxides of the $La_{1-x}Bi_xMn_2O_5$ ($x = 0.2$, 0.4, 0.6, 0.8) series were prepared in polycrystalline form using very reactive citrate precursors obtained by a soft-chemistry procedure. Stoichiometric amounts of analytical grade Bi_2O_3, La_2O_3 and $MnCO_3$ were dissolved in citric acid, adding some droplets of HNO_3 to facilitate the dissolution of the rare-earth oxide. The citrate solution was slowly evaporated, leading to an organic resin which was dried at 120 °C and then slowly decomposed at temperatures up to 600 °C in air. Subsequently, the members of the series with $x \leq 0.4$ were obtained by heating the precursors at 1000 °C for 12 h in air; the samples with $x > 0.4$ were obtained under high oxygen pressure. The precursors were slowly heated up to 900 °C at a final pressure of 200 bar, and held at this temperature for 12 h. The products were finally cooled, under pressure, at 300 °C h^{-1} down to room temperature. Finally, the oxygen pressure was slowly released. High oxygen pressure treatments were performed in a VAS furnace. About 2 g of the precursor powder was contained in a gold can during the oxygenation process.

The initial characterization of the samples was carried out by laboratory x-ray diffraction in a Bruker-axs D8 diffractometer (40 kV, 30 mA), controlled by DIFFRACT^{plus} software, in the Bragg–Brentano reflection geometry with Cu Kα radiation ($\lambda = 1.5418$ Å) and a PSD detector. Neutron powder diffraction (NPD) data were collected in the 3T2 high-resolution diffractometer ($\Delta 2\theta = 0.05°$, $\lambda = 1.2252$ Å) at room temperature and in the multidetector G4.1 diffractometer ($\Delta 2\theta = 0.1°$, $\lambda = 2.4226$ Å, for 1.5 K $\leq T \leq$ 150 K) for the study of the thermal evolution. Both instruments are installed at the Laboratoire Léon Brillouin in Saclay (France). About 4 g of sample was placed in a vanadium can; the counting time was 12 h. The neutron patterns were analyzed by the Rietveld method [19] using the Fullprof program [20]. The peak profiles were fitted by the Thompson–Cox–Hastings pseudo-Voigt function corrected for axial divergence asymmetry. The following parameters were refined in the final run of the fit: scale factor, background coefficients, zero-point error, unit-cell parameters, pseudo-Voigt corrected for asymmetry parameters, positional coordinates, and isotropic displacement factors.

Dc magnetic susceptibility was measured using a SQUID magnetometer from Quantum Design, in the temperature range from 2 to 295 K under a magnetic field of 1 kOe; isothermal magnetization measurements were carried out at $T = 2$ K for magnetic fields -50 kOe $\leq H \leq 50$ kOe.

The samples used for neutron measurements are the same as for magnetization and XRD.

3. Results

$La_{1-x}Bi_xMn_2O_5$ oxides were obtained as dark brown, polycrystalline powders. Figure 1 shows the XRD patterns, which can be indexed in an orthorhombic unit cell, isostructural to $LaMn_2O_5$ and $BiMn_2O_5$, previously reported [4, 12]. No additional peaks are observed that could indicate the presence of impurities or changes in the symmetry.

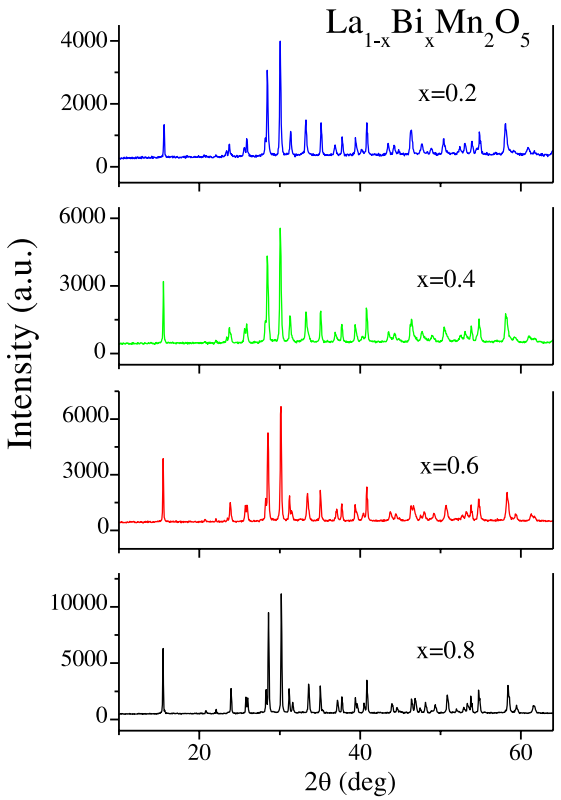

Figure 1. XRD patterns (Cu Kα) for $La_{1-x}Bi_xMn_2O_5$ oxides ($x = 0.2, 0.4, 0.6, 0.8$) indexed in the *Pbam* orthorhombic space group.

3.1. Crystallographic structure

The crystallographic structure of the series has been refined from NPD room-temperature 3T2 data in the orthorhombic space group *Pbam* (no. 55), taking as starting point the structural model of $LaMn_2O_5$. It was assumed that the Mn atoms occupy the 4f $(0, 1/2, z)$ and 4h $(x, y, 1/2)$ sites, La and Bi atoms the 4g $(x, y, 0)$ position, with different occupancies in each member of the series, and the oxygen atoms are in four different sites 4e, 4g, 4h and 8i. A view of the crystal structure is displayed in figure 2. It can be described as infinite chains of edge sharing $Mn^{4+}O_6$ octahedra arranged along the *c* axis, with the chains linked by pairs of $Mn^{3+}O_5$ corner sharing pyramids (pyramid dimers). Mn^{4+}(Mn1) are thus located in a distorted octahedral environment. These $Mn^{4+}O_6$ octahedra share edges via O2 and O3 oxygens and they are interconnected with the pyramids by O3 and O4. Mn^{3+}(Mn2) are placed in distorted tetragonal pyramids. These $Mn^{3+}O_5$ pyramids contain different Mn^{3+}–O bond lengths: four oxygen atoms (two O1 and two O4) are in a square-planar configuration and one O3 is in the axial position. Within the dimers, the two O1 atoms connect the pyramids with each other (sharing edges) and the two O4 connect one pyramid with two octahedra. Finally, the fifth oxygen (O3) is in the axial position at a longer distance and it is also connected to two MnO_6 octahedra. The $(La/Bi)O_8$ units can be described as bicapped trigonal prisms.

The lattice parameters, atomic positions, displacement parameters and the corresponding discrepancy factors

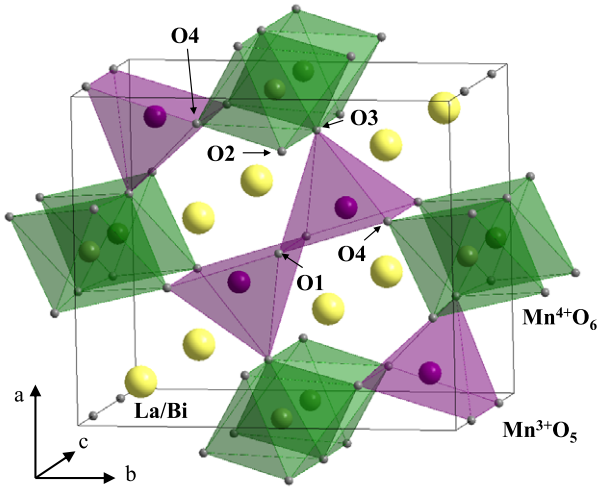

Figure 2. View of the crystallographic structure of $La_{1-x}Bi_xMn_2O_5$ along the *c* axis. Octahedra and tetragonal pyramids correspond to $Mn^{4+}O_6$ and $Mn^{3+}O_5$ polyhedra. The octahedra share edges, forming infinite chains along the *c* axis. The pyramids form dimer units, linking together the chains of octahedra. The larger yellow spheres represent the La/Bi atoms.

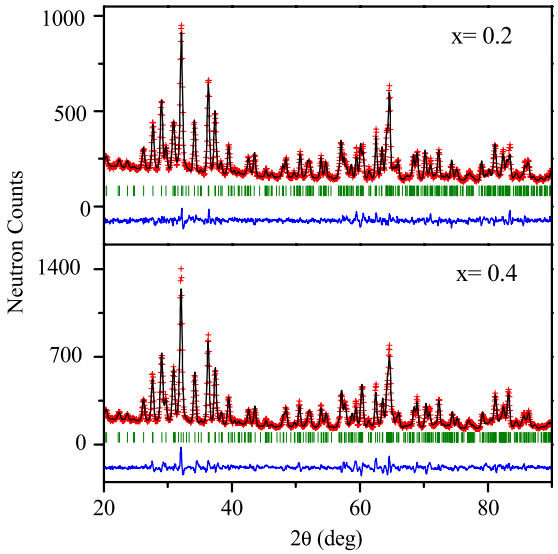

Figure 3. Observed (crosses), calculated (full line) and difference (bottom line) NPD Rietveld profiles at RT of $La_{0.8}Bi_{0.2}Mn_2O_5$ and $La_{0.6}Bi_{0.4}Mn_2O_5$ oxides.

obtained after the refinement of the structures at 295 K are shown in table 1. The most characteristic atomic distances and bonding angles are presented in tables 2 and 3. The good agreement between the observed and calculated NPD patterns at room temperature in the final Rietveld fit can be appreciated in figures 3 and 4. Figure 5 depicts the evolution of the unit-cell dimensions and volume as the bismuth content increases. The values of the unit-cell parameters of the parent $LaMn_2O_5$ and $BiMn_2O_5$ oxides have been taken from [4, 13] respectively.

Table 1. Unit cell, positional, thermal parameters and ordered magnetic moments for $La_{1-x}Bi_xMn_2O_5$ defined in the orthorhombic *Pbam* (No. 55) space group, $Z = 4$, from NPD data at 295 K. La/Bi and O2 atoms are at 4g (x, y, 0) positions; Mn1 at 4f (0, 1/2, z); Mn2 and O3 at 4h (x, y, 1/2); O1 at 4e (0, 0, z) and O4 at 8i (x, y, z) positions.

x	0.2	0.4	0.6	0.8
a (Å)	7.6494(4)	7.6328(6)	7.6006(5)	7.5738(3)
b (Å)	8.6742(5)	8.6563(7)	8.6101(6)	8.5706(3)
c (Å)	5.7243(3)	5.7372(4)	5.7441(3)	5.7530(2)
V (Å^3)	379.82(4)	379.07(5)	375.91(4)	373.44(3)
La/Bi				
Occupied La/Bi				
x	0.1460(5)	0.1494(5)	0.1512(5)	0.1551(3)
y	0.1722(4)	0.1714(4)	0.1698(4)	0.1671(3)
B (Å^2)	0.46(6)	0.59(6)	0.50(6)	0.70(4)
Mn1				
z	0.257(2)	0.26(2)	0.26(1)	0.2617(9)
B (Å^2)	0.5(1)	0.3(1)	0.47(9)	0.35(6)
Mn2				
x	0.406(1)	0.403(1)	0.403(9)	0.4059(6)
y	0.3517(8)	0.3517(8)	0.353(7)	0.3518(5)
B (Å^2)	0.3(1)	0.2(1)	0.1(1)	0.43(7)
O1				
z	0.278(1)	0.280(1)	0.278(10)	0.2820(7)
B (Å^2)	0.60(8)	0.54(8)	0.84(8)	0.95(6)
O2				
x	0.1527(4)	0.1532(7)	0.153(7)	0.1547(5)
y	0.4492(6)	0.447(6)	0.447(5)	0.4462(4)
B(Å^2)	0.39(8)	0.30(8)	0.56(8)	0.61(6)
O3				
x	0.1502(8)	0.1514(8)	0.149(8)	0.1463(5)
y	0.4348(6)	0.4347(6)	0.430(5)	0.4270(4)
B (Å^2)	0.48(8)	0.56(9)	0.49(8)	0.36(5)
O4				
x	0.4043(4)	0.4007(4)	0.393(3)	0.3893(2)
y	0.2054(4)	0.2047(4)	0.203(4)	0.2010(3)
z	0.2550(7)	0.2561(7)	0.256(7)	0.2552(5)
B (Å^2)	0.48(5)	0.33(6)	0.57(5)	0.63(4)
Reliability factors				
χ^2	2.16	3.85	3.61	1.75
R_p (%)	3.77	4.90	4.55	3.24
R_{wp} (%)	4.75	6.13	5.78	4.01
R_{exp}	3.23	3.12	3.04	3.03
R_I (%)	5.36	5.46	4.84	4.19

3.2. Magnetic properties

The dc magnetic susceptibility versus temperature curves for $La_{1-x}Bi_xMn_2O_5$, $x = 0.0$, 0.2, 0.4, 0.6, 0.8, 1.0 are displayed in figure 6(a) (data for $x = 0.0$ and 1.0 members are taken from [11, 13]). The La-rich members with $x = 0.2$ and 0.4 show a similar behavior to that of $x = 0$, $LaMn_2O_5$, displaying a broad maximum centered around 40 K, ascribed to the long-range ordering temperature, and a thermomagnetic irreversibility between the ZFC and FC curves for temperatures below the ordering transition temperature. This divergence between both curves has been previously reported for $LaMn_2O_5$ and has been attributed to the formation of a spin-glass state [11]. For the Bi-rich compounds with $x = 0.6$ and 0.8 a distinct evolution of the susceptibility is observed: a first broad maximum is followed, below 50 K, by an abrupt increase of the magnetization, immediately followed by a dramatic split of the ZFC and FC curves. The maximum in ZFC susceptibility is ascribed to the onset of ferromagnetic ordering of a small fraction of Mn_3O_4 spinel, previously undetected by diffraction methods, whereas the previous shoulder is probably due to the establishment of the 3D magnetic structure of the main phase, as will be discussed later on.

The hysteresis loops (figure 6(b)) observed for $La_{1-x}Bi_xMn_2O_5$, ($x = 0.6$ and 0.8) are characteristic of an antiferromagnetic behavior with some overlapped ferromagnetic response. As will be shown in the magnetic structure, the ordering for all of the $La_{1-x}Bi_xMn_2O_5$ compounds is antiferromagnetic. However, in the compounds $x = 0.6$ and 0.8 the presence of a Mn_3O_4 minor impurity, ferromagnetic below $T_C = 43$ K [21, 22], accounts for the ferromagnetic component observed in the magnetization measurements. As commented before, the Mn_3O_4 ferromagnetic transition was observed in figure 6(a), where for $x = 0.6$ and 0.8 a sharp increase of the magnetization occurs around 43 K, matching

Table 2. Main interatomic distances (Å) for the $La_{1-x}Bi_xMn_2O_5$ series.

x	0.2	0.4	0.6	0.8
$R^{3+}O_8$ bicapped prism				
La/Bi–O1(x2)	2.453(5)	2.465(5)	2.452(5)	2.462(3)
La/Bi–O2	2.403(6)	2.389(6)	2.385(6)	2.391(4)
La/Bi–O2	2.472(6)	2.456(6)	2.427(6)	2.380(4)
La/Bi–O4(x2)	2.473(5)	2.433(5)	2.371(4)	2.321(3)
La/Bi–O4(x2)	2.584(5)	2.629(5)	2.686(4)	2.736(3)
⟨La/Bi–O⟩	2.487(5)	2.487(5)	2.479(5)	2.476(3)
$Mn^{4+}O_6$ octahedra				
Mn1–O2(x2)	1.928(7)	1.950(8)	1.964(7)	1.963(5)
Mn1–O3(x2)	1.892(7)	1.884(8)	1.871(7)	1.870(5)
Mn1–O4(x2)	1.926(3)	1.927(3)	1.924(3)	1.915(2)
⟨Mn1–O⟩	1.915(6)	1.920(6)	1.920(6)	1.916(4)
$Mn^{3+}O_5$ tetragonal pyramid				
Mn2–O1(x2)	1.945(7)	1.949(7)	1.936(6)	1.922(4)
Mn2–O3	2.09(1)	2.05(1)	2.039(9)	2.070(6)
Mn2–O4(x2)	1.891(6)	1.891(6)	1.914(6)	1.916(4)
⟨Mn2–O⟩	1.952(7)	1.946(5)	1.948(7)	1.949(5)
Mn–Mn distances				
Mn1–Mn1	2.94(1)	2.99(1)	3.02(1)	3.011(7)
Mn1–Mn1	2.79(1)	2.75(1)	2.72(1)	2.742(7)
Mn2–Mn2	2.95(1)	2.97(1)	2.924(9)	2.913(6)

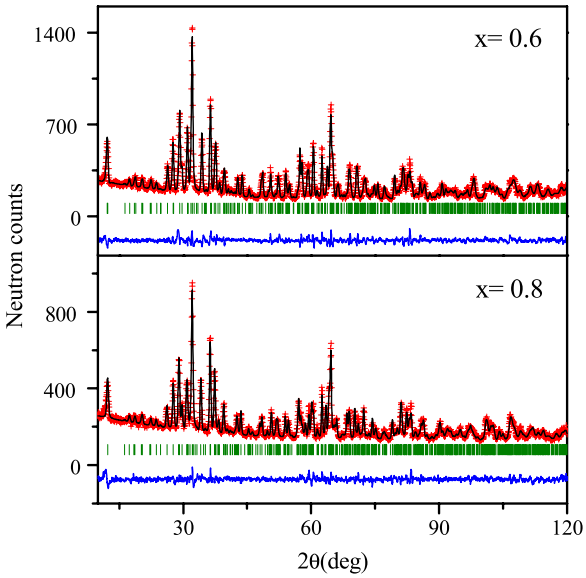

Figure 4. Observed (crosses), calculated (full line) and difference (bottom line) NPD Rietveld profiles at RT of $La_{0.4}Bi_{0.6}Mn_2O_5$ and $La_{0.2}Bi_{0.8}Mn_2O_5$ oxides.

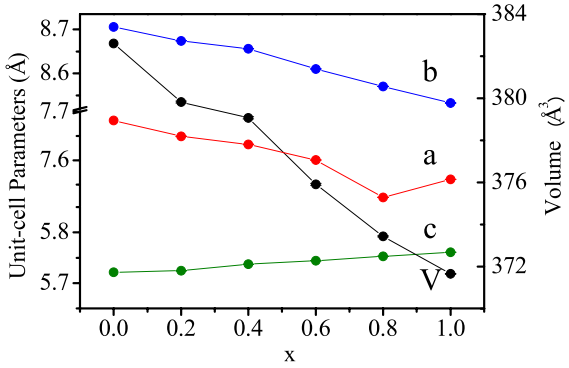

Figure 5. (a) Variation of the cell parameters and the unit-cell volume when x increases. (Results for $x = 0$, 1 were taken from [4, 13] respectively.)

the magnetic ordering transition of Mn_3O_4. In the case of $x = 0.2$ and 0.4 the small ferromagnetic component could be ascribed to spin canting or short-range ferromagnetic interactions, as has been previously observed in many other similar oxides [23].

3.3. Magnetic structure

The magnetic structures of $La_{1-x}Bi_xMn_2O_5$ ($x = 0.2$, 0.4, 0.6, 0.8) have been analyzed from a set of neutron diffraction patterns acquired in the temperature interval 1.5 K $< T <$ 150 K at a wavelength $\lambda = 2.4226$ Å. In the magnetic structure resolution, the magnetic structures of $LaMn_2O_5$ [11] and $BiMn_2O_5$ [13, 14] have been taken into consideration. The Rietveld plots after the refinement of the magnetic structures at 1.5 K are shown in figure 7.

3.3.1. La-rich compounds; $x = 0.2, 0.4$. For $La_{0.8}Bi_{0.2}Mn_2O_5$ and $La_{0.6}Bi_{0.4}Mn_2O_5$, on decreasing the temperature below 25 K, new peaks appear in the diffraction patterns, which can be indexed with the propagation vector $\mathbf{k}_1 = (0, 0, 1/2)$. Their magnetic structures are defined by the same propagation vector as in $LaMn_2O_5$. Figure 8 shows the thermal evolution of the magnetic reflection $(1, 1, 1/2)$ for both La-rich compounds, indicating in both cases that the transition temperature T_N is around 25 K.

After checking the different solutions obtained by the group theory technique for $LaMn_2O_5$ [11], the best agreement is obtained for the same magnetic coupling as in $LaMn_2O_5$, $(G_x, A_y, 0)$ for Mn1 atoms (site 4h) and $(0, 0, C'_z)$ for Mn2

Table 3. Selected bond angles (°) for the $La_{1-x}Bi_xMn_2O_5$ series.

x	0.2	0.4	0.6	0.8
O2–Mn1–O2	80.7(4)	80.1(4)	79.3(4)	79.8(3)
O2–Mn1–O3	97.2(3)	97.0(3)	97.1(3)	97.5(2)
	175.7(4)	175.6(5)	174.3(4)	174.0(3)
O2–Mn1–O4	90.9(3)	90.7(3)	91.3(3)	92.0(2)
	88.7(3)	88.3(3)	86.8(3)	86.3(2)
O3–Mn1–O3	85.2(5)	86.2(5)	86.8(5)	85.7(3)
O3–Mn1–O4	87.6(4)	88.5(4)	88.9(3)	88.4(2)
	92.8(4)	92.5(4)	93.0(3)	93.2(2)
O4–Mn1–O4	179.4(3)	178.6(3)	177.5(3)	177.8(2)
O1–Mn2–O1	81.5(4)	80.9(4)	82.1(4)	81.5(3)
O1–Mn2–O3	96.8(4)	97.2(4)	98.5(4)	98.4(3)
O1–Mn2–O4	87.9(3)	88.1(3)	88.6(3)	89.5(2)
	158.5(4)	157.8(4)	159.8(4)	161.8(3)
O3–Mn2–O4	103.0(4)	103.2(4)	100.5(4)	98.5(3)
O4–Mn2–O4	95.7(4)	95.4(4)	94.3(3)	94.6(2)
Mn2–O1–Mn2	98.5(5)	99.1(59)	97.9(5)	98.5(3)
Mn1–O2–Mn1	99.3(6)	99.9(7)	100.7(6)	100.2(4)
Mn1–O3–Mn1	94.8(6)	93.8(7)	93.2(6)	94.3(4)
Mn1–O3–Mn2	132.3(5)	132.8(6)	132.7(5)	131.8(4)
Mn1–O4–Mn2	127.9(4)	127.3(4)	125.6(4)	124.3(3)

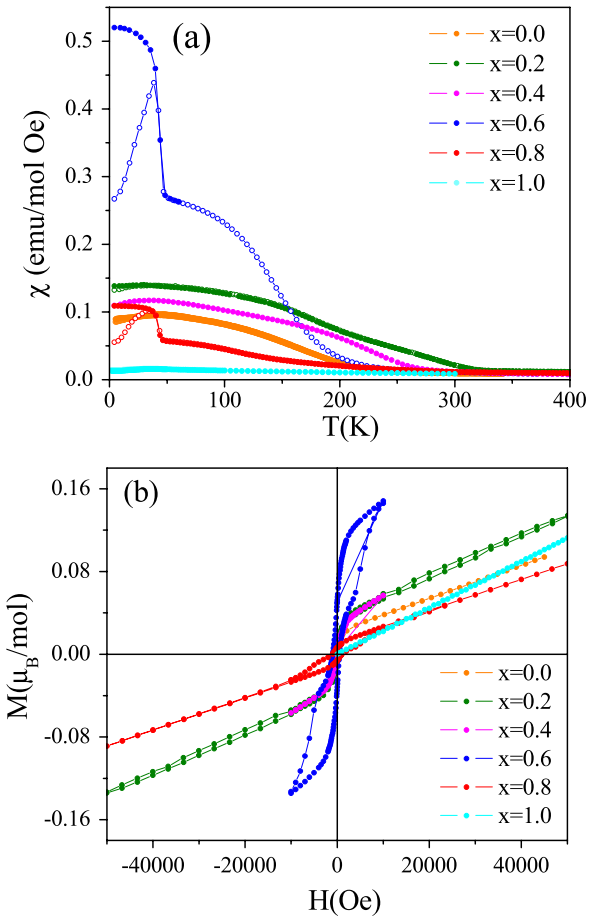

Figure 6. (a) Thermal evolution of the field cooling (FC) and zero field cooling (ZFC) dc susceptibility of $La_{1-x}Bi_xMn_2O_5$ oxides ($x = 0$, 0.2, 0.4, 0.6, 0.8, 1). Upper inset: reciprocal susceptibility (FC data). (b) Magnetization versus magnetic field isotherms at $T = 2$ K. (Results for $x = 0$, 1 were taken from [4, 13] respectively.)

atoms (site 4f). A schematic view of the magnetic structure is presented in figure 9. Along the direction of the octahedral chains (along the c axis) the octahedra are interleaved either by a layer of La^{3+}/Bi^{3+} ions or by a layer of Mn^{3+} ions. As shown in figure 9, Mn^{4+} ions in the octahedra are situated at the $z = 1 - z_0$, z_0, and $-z_0$ planes. Intercalated between them, there are planes of Mn^{3+} ions at $z = 1/2$ and interleaved planes of La^{3+}/Bi^{3+} ions at $z = 0$. This implies that, for a given MnO_6 octahedron, there are two closer MnO_6 octahedra: one at $d = 2z_0$ (separated by La^{3+}/Bi^{3+} ions) and another at $d = 1–2z_0$ (separated by Mn^{3+} ions). The MnO_5 units in the layers between the octahedra also play an important role in the magnetic coupling between neighboring MnO_6 chains and also between the MnO_5 pyramids themselves. The magnetic moments of the Mn^{4+} ions are directed along c in the octahedra chains. Within a single chain of octahedra, the coupling between the Mn^{4+} ions of two adjacent octahedra separated by a La^{3+}/Bi^{3+} layer is ferromagnetic, whereas those separated by a Mn^{3+} layer are antiferromagnetically coupled. Thus, we have alternating FM and AFM couplings along the chains. Within the dimer units of $Mn^{3+}O_5$ pyramids, the two Mn^{3+} spins also show an AFM coupling, with the magnetic moments lying in the *ab* plane, in such a way that the magnetic moment direction is nearly perpendicular to the base of the pyramid. The thermal evolution of the magnetic moments for $x = 0.2$ and 0.4 is represented in figures 10(a) and (b), respectively. As is shown in table 4, at 1.5 K, the magnetic moments for $La_{0.8}Bi_{0.2}Mn_2O_5$ are 1.58(8) μ_B and 1.84(7) μ_B for Mn1 and Mn2, respectively. For $La_{0.6}Bi_{0.4}Mn_2O_5$ the magnetic moments are 1.52(8) μ_B and 1.21(10) μ_B for Mn1 and Mn2, respectively.

Table 4. Results obtained from the fitting of the magnetic structure at $T = 1.5$ K. The solutions are $(G_x, A_y, 0)$ and $(0, 0, C'_z)$ for Mn(4h) and Mn(4f), respectively.

	Mn(4h)	Mn(4f)
$La_{0.8}Bi_{0.2}Mn_2O_5$		
m_x, m_y, m_z (μ_B)	1.55(7), −0.98(11), 0	0, 0, 1.58(8)
$\|\mathbf{m}\|$ (μ_B)	1.84(7)	1.58(8)
Discrepancy factors	$R_{Bragg} = 3.9$; $R_{Mag} = 12.0$,	$\chi^2 = 2.4$
$La_{0.6}Bi_{0.4}Mn_2O_5$		
Values (m_x, m_y, m_z) (μ_B)	0.96(11), −0.73(13), 0	0, 0, 1.52(8)
$\|\mathbf{m}\|$ (μ_B)	1.21(10)	1.52(8)
Discrepancy factors	$R_{Bragg} = 4.3$; $R_{Mag} = 13.3$,	$\chi^2 = 5.8$

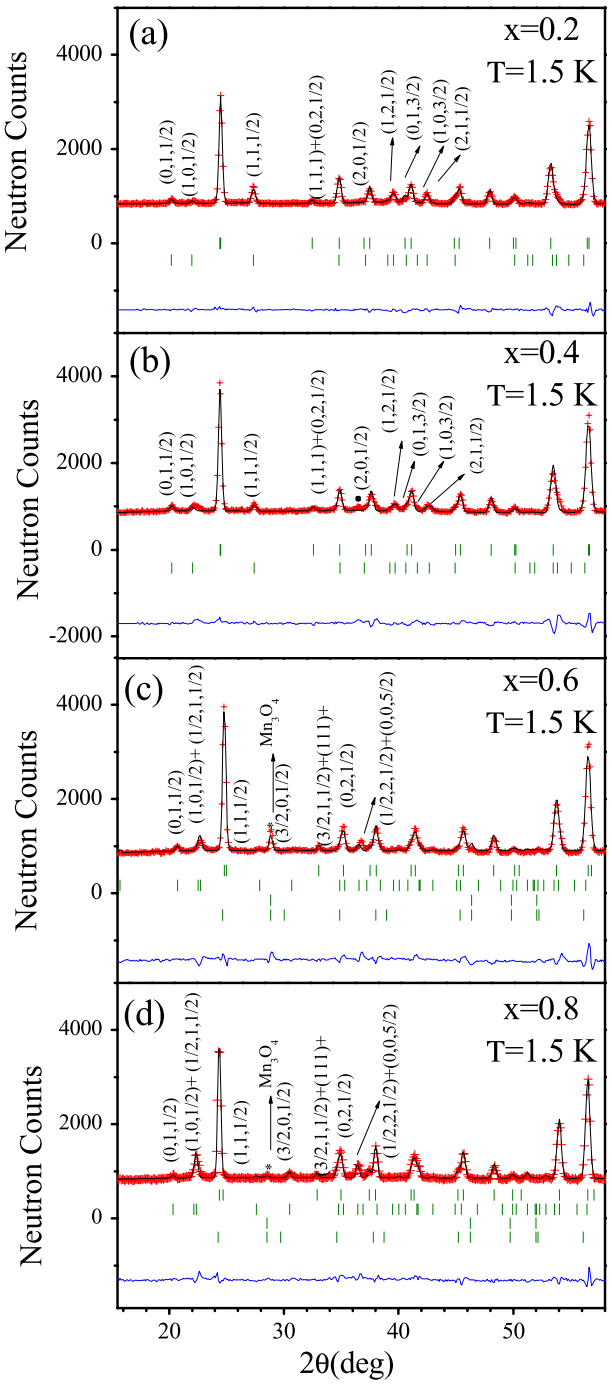

Figure 7. Observed (crosses), calculated (full line) and difference (bottom line) NPD patterns corresponding to $T = 1.5$ K data. The first series of tick marks corresponds to the crystallographic reflections. The magnetic reflections correspond to the propagation vectors $\mathbf{k}_1 = (0, 0, 1/2)$ (second series) and $\mathbf{k}_2 = (1/2, 0, 1/2)$ (fourth series). For $x = 0.4$ the magnetic reflection marked with • corresponds to $\mathbf{k}_2 = (1/2, 0, 1/2)$. For $x = 0.6$ and 0.8 the magnetic reflection marked with * corresponds to Mn_3O_4 (third series).

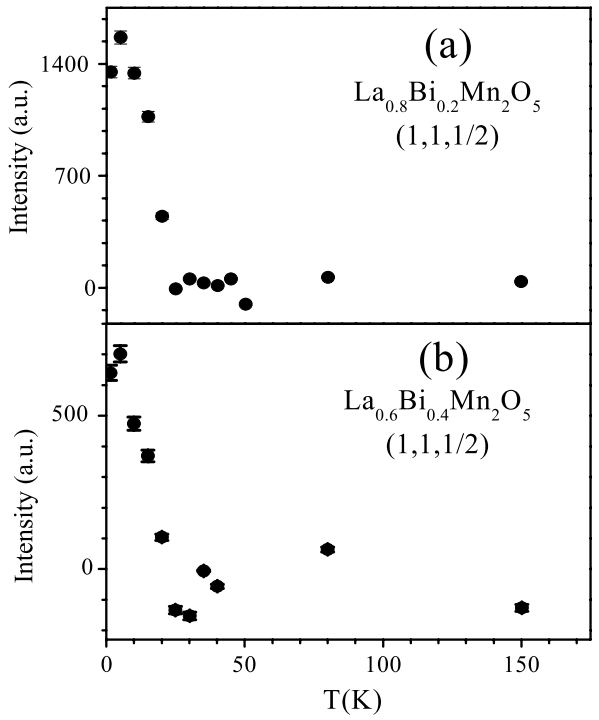

Figure 8. Thermal evolution of the magnetic reflection (1, 1, 1/2) for the La-rich compounds $La_{0.8}Bi_{0.2}Mn_2O_5$ (a) and $La_{0.6}Bi_{0.4}Mn_2O_5$ (b).

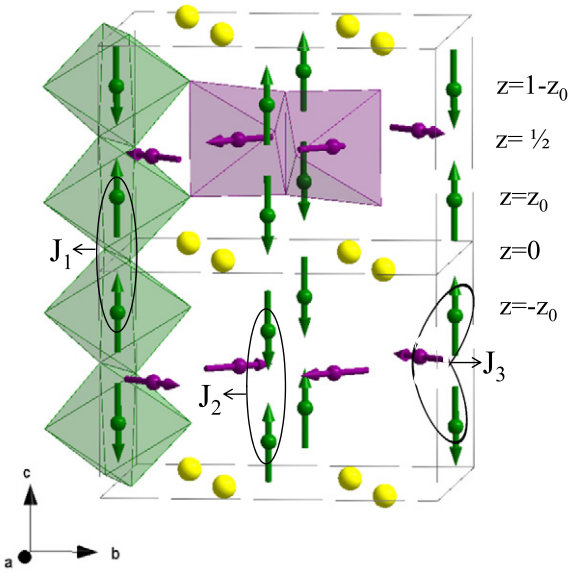

Figure 9. Schematic view of the magnetic structure of the La-rich compounds $La_{0.8}Bi_{0.2}Mn_2O_5$ and $La_{0.6}Bi_{0.4}Mn_2O_5$. The different magnetic interactions between Mn^{4+} cations are schematized in the figure: J_1 represents the superexchange interaction between Mn^{4+} ions separated by La/Bi layers, across Mn^{4+}–O2–Mn^{4+} paths, J_2 represents the superexchange interaction between Mn^{4+} ions separated by Mn^{3+} layers, across the direct superexchange path Mn^{4+}–O3–Mn^{4+}, and J_3 represents interactions across the indirect superexchange path Mn^{4+}–O2–Mn^{3+}–O4–Mn^{4+}.

It is worth indicating that, as shown in figure 7(b), for $La_{0.6}Bi_{0.4}Mn_2O_5$ two small additional magnetic peaks are observed in the 1.5 K patterns that cannot be indexed with $\mathbf{k}_1 = (0, 0, 1/2)$. However, they can be indexed with $\mathbf{k}_2 = (1/2, 0, 1/2)$, which corresponds to the propagation vector of the magnetic structure of $BiMn_2O_5$. Therefore, for this intermediate composition we indeed observe an admixture of the magnetic structures of both end members.

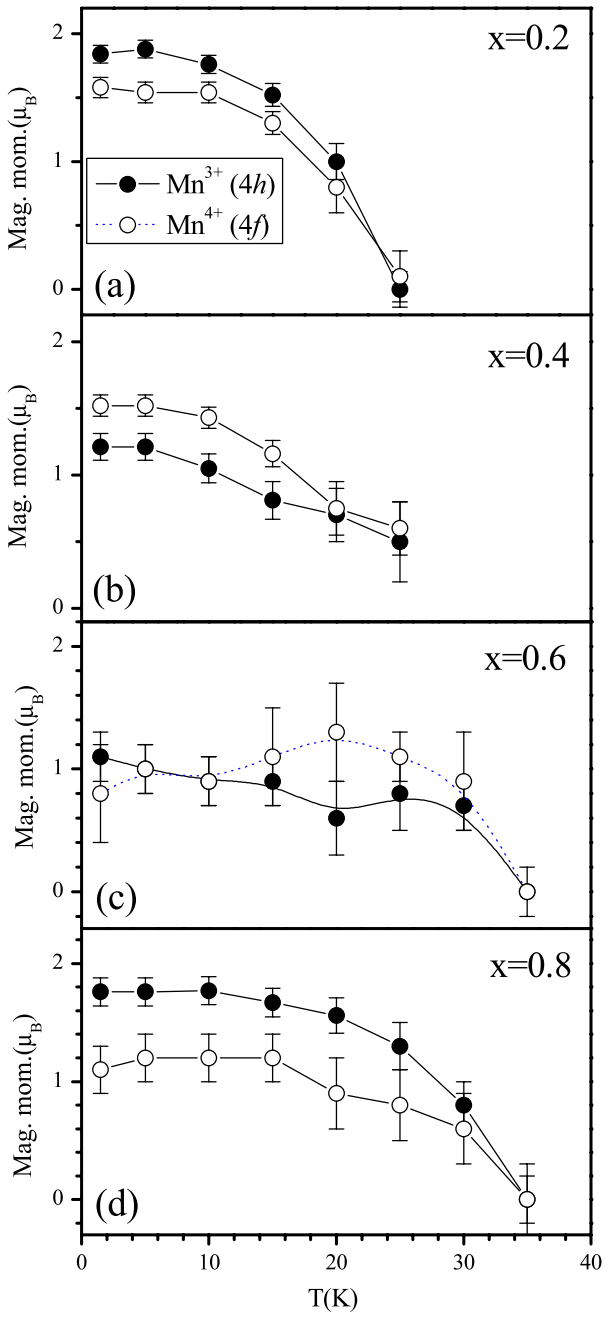

Figure 10. Thermal evolution of the magnetic moments for (a) $La_{0.8}Bi_{0.2}Mn_2O_5$, (b) $La_{0.6}Bi_{0.4}Mn_2O_5$, (c) $La_{0.4}Bi_{0.6}Mn_2O_5$ and (d) $La_{0.2}Bi_{0.8}Mn_2O_5$.

3.3.2. Bi-rich compounds, $x = 0.6$, 0.8. For the Bi-rich compounds the magnetic structure is more complex. Both for $La_{0.4}Bi_{0.6}Mn_2O_5$ and $La_{0.2}Bi_{0.8}Mn_2O_5$, on decreasing the temperature below 35 K, new peaks appear that can be indexed by using both propagation vectors $\mathbf{k}_1$ and $\mathbf{k}_2$. Also, as shown in figures 7(c) and (d), an additional peak at 28° is observed. This peak, which is already observed at 35 K, corresponds to the strongest magnetic reflection (101) of Mn_3O_4. Mn_3O_4 is a tetragonal spinel with a ferromagnetic ordering below $T_C = 43$ K. Its magnetic unit cell (a, $2a$, c) is double the size of the chemical unit cell [22, 23].

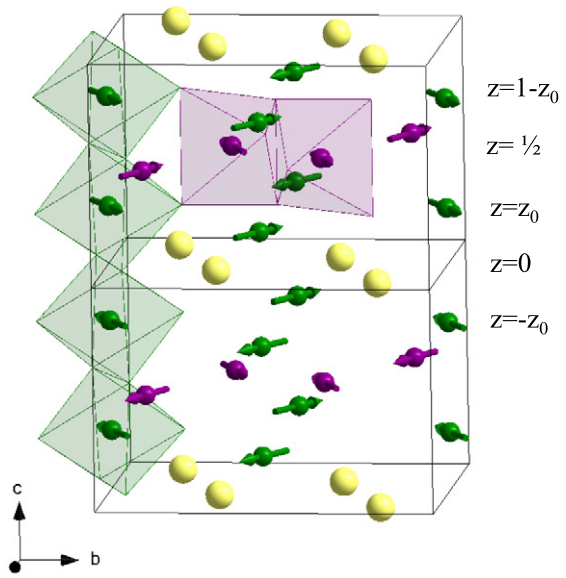

Figure 11. Schematic view of the magnetic structure of the Bi-rich compounds $La_{0.4}Bi_{0.6}Mn_2O_5$ and $La_{0.2}Bi_{0.8}Mn_2O_5$.

The magnetic structures of the Bi-rich compounds have been modeled by considering that the solution for $\mathbf{k}_1$ is given by the same spin arrangement as that of the La-rich compounds, and for $\mathbf{k}_2$ the solution is the same as that for $BiMn_2O_5$. Actually, as the Bi content increases the peaks corresponding to the propagation vector $\mathbf{k}_1$ become smaller and the ones related to $\mathbf{k}_2$ increase in intensity. Following the notation given in [8], the magnetic structure corresponding to $\mathbf{k}_2$ is $(F_x, C_y, 0)$ for the Mn2 atoms in the 4h site, and $(G'_x, A'_y, 0)$ for the atoms Mn1 in the 4f site. For this magnetic structure all the magnetic moments are contained in the *ab* plane. A schematic view of their magnetic structure is presented in figure 11. In this case the $z = z_0$ and $-z_0$ Mn^{4+} planes are separated by a La^{3+}/Bi^{3+} plane and the coupling between them is AFM; conversely, between the $z = 1 - z_0$ and z_0 Mn^{4+} planes, separated by a Mn^{3+} plane, they are coupled ferromagnetically. Within each Mn plane, for both Mn^{3+} and Mn^{4+} sublattices, the coupling along the *b* direction is FM and along the *a* direction it is AFM. In the Mn^{3+} planes, the ions related by an inversion center are antiferromagnetically coupled. At 1.5 K, the magnetic moments for $La_{0.4}Bi_{0.6}Mn_2O_5$ are 0.8(2) μ_B and 1.1(2) μ_B for Mn1 and Mn2, respectively, while for $La_{0.2}Bi_{0.8}Mn_2O_5$ they are 1.1(2) μ_B and 1.76(12) μ_B. Figures 10(c) and (d) show the thermal evolution of the magnetic moments for $x = 0.6$ and 0.8 respectively, indicating that the ordering temperature for both samples is around $T_N = 35$ K.

The thermal evolution of the lattice parameters a and c for the La-rich and Bi-rich compounds is presented in figure 12. For $x = 0.2$ (figure 12(a)) and 0.4 (figure 12(b)), a and c lattice parameters present an anomaly around 25 K, coincident with the establishment of the magnetic ordering. In both cases, upon warming, the compounds exhibit an unusual contraction of the a parameter as the temperature increases below T_N. For the Bi-rich compounds, $La_{0.4}Bi_{0.6}Mn_2O_5$ and

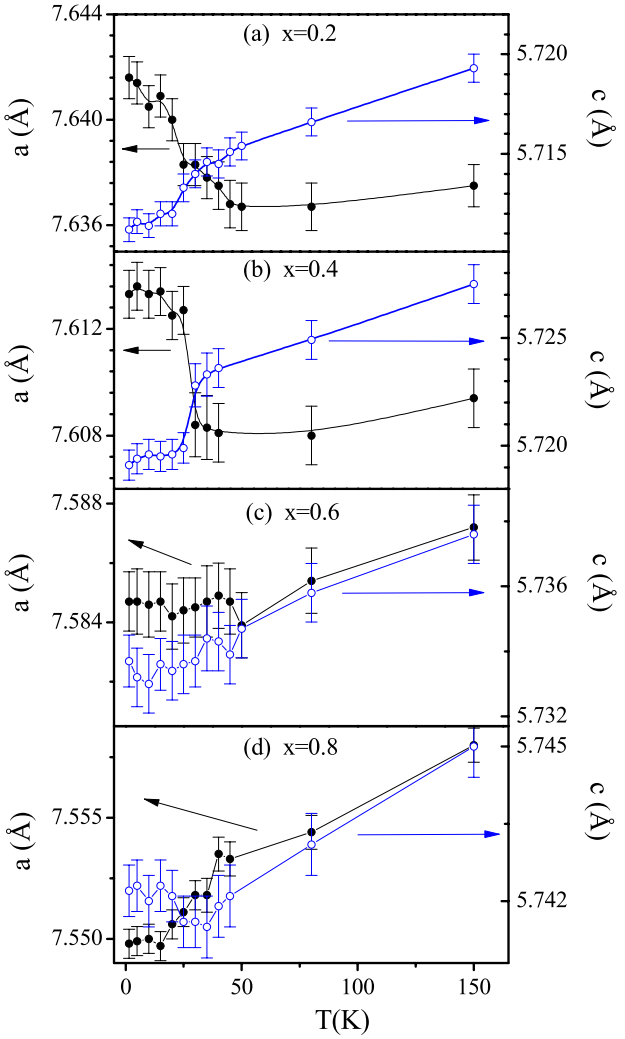

Figure 12. Thermal evolution of the *a* and *c* lattice parameters for (a) $La_{0.8}Bi_{0.2}Mn_2O_5$, (b) $La_{0.6}Bi_{0.4}Mn_2O_5$, (c) $La_{0.4}Bi_{0.6}Mn_2O_5$ and (d) $La_{0.2}Bi_{0.8}Mn_2O_5$.

$La_{0.2}Bi_{0.8}Mn_2O_5$, the *a* parameter increases with temperature in the whole range of temperature measured; these compounds present no significant anomaly around the magnetic ordering temperature, $T_N = 35$ K. Only for $La_{0.2}Bi_{0.8}Mn_2O_5$ is there a small contraction of the *c* parameter below T_N.

4. Discussion

The complete series of compounds $La_{1-x}Bi_xMn_2O_5$ ($x = 0.2$, 0.4, 0.6, 0.8) is isotypic with both end members, $LaMn_2O_5$ and $BiMn_2O_5$. The evolution of the unit-cell parameters shows a constant reduction of *a*, *b* and *V* when the content of Bi increases, while a slight increment of *c* parameter occurs (figure 5). The global decrease of the unit-cell size cannot be explained using the values of the ionic radii, since the ionic radius of Bi^{3+} (1.20 Å) is greater than that of La^{3+} (1.16 Å) [24]. The presence of a Bi^{3+} electron lone pair is responsible for the anomalous variation of the unit-cell size. This will be discussed subsequently in connection with the variation of the La/Bi–O bond lengths since an increment of the anisotropy has been found as the content of Bi (*x*) increases. The effect of the lone pair of Bi has been previously reported in other related oxides, such as $BiMn_2O_5$ or $BiFeMnO_5$ [13, 25]. Moreover, the structural effect of the lone pair of other *p*-block elements, such as Pb^{2+}, Se^{4+} or Te^{4+}, providing extremely distorted coordination environments around these atoms, has been recently addressed for Pb_2ScSbO_6 [26], Pb_2TmSbO_6 [27], $SeMnO_3$ [28] or $TeNiO_3$ [29].

When *x* increases the (La/Bi)O_8 polyhedra become more distorted. A coupled shift of the Bi position along the [110] direction is observed with respect to the position of lanthanum cations. As a consequence, the difference between the two La/Bi–O4 distances increases. La/Bi–O4 distances (table 2) decrease or increase along the series from 2.473(5) Å for $x = 0.2$ to 2.321(3) Å for $x = 0.8$ and from 2.584(5) Å for $x = 0.2$ to 2.736(3) Å for $x = 0.8$. The distortion of this coordination environment is a result of the presence of the lone electron pair on Bi^{3+}. The repulsion of the lone pair leads to an asymmetric distribution of the Bi–O bonds, involving significant shifts of some oxygen positions.

The mentioned oxygen shifts indirectly lead to important changes in Mn–O distances. In particular, the $Mn1O_6$ octahedron becomes more distorted when *x* increases, the three Mn1–O distances becoming increasingly different from each other. The substitution of La by Bi produces an unusual increment of Mn1–O2 distances, achieving values for $x = 0.8$ and 1.0 [13] higher than any other RMn_2O_5 compound (table 2). However, Mn1–O3 and Mn1–O4 slightly decrease when *x* increases. This huge increment of Mn1–O2 distances compared to the slight decrease of Mn1–O3 could partially explain the increment of the *c* parameter as the content of Bi is enhanced, whereas the diminution of Mn1–O4 is the origin of the reduction of the *a* and *b* parameters (see figure 5). $Mn2O_5$ pyramids are less affected by the Bi substitution: Mn2–O1 distances decrease along the series whereas Mn2–O4 bond lengths increase, again reaching values higher than any other RMn_2O_5 oxide; Mn2–O3 decreases, scaling with the decrease of the *a* parameter.

These differences in the interatomic distances will play an important role in the different spin arrangements along the series. As *x* increases the magnetic propagation vector changes from $\mathbf{k}_1 = (0, 0, 1/2)$ to $\mathbf{k}_2 = (1/2, 0, 1/2)$ and thus the orientation of the magnetic moments also evolves. In these compounds we have two different magnetic moments in two different positions: Mn^{4+} in octahedral sites and Mn^{3+} in corner sharing pyramids. There are different magnetic interactions to take into account: (a) superexchange interactions between the Mn^{4+} ions separated by an La^{3+}/Bi^{3+} layer, across an Mn^{4+}–O2–Mn^{4+} (Mn1–O2–Mn1) path assigned to the J_1 superexchange parameter; (b) the superexchange interaction between the Mn^{4+} ions separated by a Mn^{3+} layer, which must be considered as an admixture of two different interactions: across the direct superexchange path Mn^{4+}–O3–Mn^{4+} (Mn1–O3–Mn1), labeled J_2, and across the indirect superexchange interaction involving the $Mn^{3+}O_5$ units, Mn^{4+}–O2–Mn^{3+}–O4–Mn^{4+} (Mn1–O2–Mn2–O4–Mn1) paths, characterized by J_3. The

different superexchange paths have been schematized in figure 9. The strength of the different magnetic interactions, FM or AFM, is related to the different bond distances and bond angles. In the case of the samples with small x ($x = 0.2$ and 0.4) the J_1 interactions are FM, and for $x = 0.6$ and 0.8 these interactions are AFM. The Mn1–Mn1 distances separated by La/Bi cation layers evolve as 2.94(1) Å for $x = 0.2$, 2.99(1) Å for $x = 0.4$, 3.02(1) Å for $x = 0.6$ and 3.011(7) Å for $x = 0.8$. Thus, it seems that the increment of the distances favors the AFM interactions. Also it is important to comment on the evolution of the angles: the Mn1–O2–Mn1 angles evolve as 99.3(6)° for $x = 0.2$, 99.9(7)° for $x = 0.4$, 100.7(6)° for $x = 0.6$ and 100.2(4)° for $x = 0.8$. Therefore, angles closer to 180° favor the AFM interactions and angles closer to 90° favor the FM interaction. These superexchange magnetic interactions can be rationalized in the Goodenough–Kanamori rules [30]. It is well known that in structures containing intermediate cation–anion–cation angles (between 180° and 90°) the sign of the magnetic interactions change from antiferromagnetic to ferromagnetic as the angles approach 90°. The direct superexchange interaction via half-occupied Mn t_{2g} orbitals would be antiferromagnetic for an ideal Mn–O–Mn angle of 180°. The microscopic reason for the appearance of such FM interactions for very bent bond angles can be found in the direct overlapping between t_{2g} orbitals of neighboring magnetic cations, giving rise to the 'delocalization superexchange' defined by Goodenough.

Concerning the superexchange interaction between the Mn^{4+} ions separated by Mn^{3+} layers (labeled as J_2 and J_3 interactions), in the case of the samples with low content of Bi, the global interaction between Mn1–Mn1 across these layers is AFM. If the indirect superexchange interaction is isotropic, J_3 would tend to couple the two Mn^{4+} ions placed at both sides of the Mn^{3+} layer ferromagnetically, as both of these Mn^{4+} ions are symmetrically arranged with respect to the Mn^{3+} layer. The experimental results indicate that the coupling is AFM, which implies that J_2 must be negative and much greater than J_3. In the case of the samples with high Bi content, the global interactions across Mn^{3+} layers are FM, so the J_2 direct interactions would be AFM and the J_3 indirect ones also AFM in such a way that the final coupling between Mn^{4+} across Mn^{3+} layers is FM. If we compare the Mn1–Mn1 distances separated by Mn^{3+} layers along the series we observe that they evolve as 2.79(1) Å for $x = 0.2$, 2.75(1) Å for $x = 0.4$, 2.72(1) Å for $x = 0.6$ and 2.742(7) Å for $x = 0.8$. Thus, J_2 and J_3 are reinforced compared to J_1 in the samples with higher values of x.

Summarizing, for all the samples the magnetic moments of Mn^{4+} along c are coupled alternately FM and AFM, but with different interactions if the octahedral layers are separated by La/Bi layers or Mn^{3+} layers, with these different magnetic interactions depending on the different angles and distances found when the Bi content increases. Regarding the orientation of the magnetic moments, in $La_{0.8}Bi_{0.2}Mn_2O_5$ and $La_{0.6}Bi_{0.4}Mn_2O_5$ the moments of Mn^{4+} ions are directed along the c direction and for $La_{0.4}Bi_{0.6}Mn_2O_5$ and $La_{0.2}Bi_{0.8}Mn_2O_5$ the moments lie in the ab plane. This could be explained as due to the magnetic anisotropy, which is mainly given by the symmetry of the ion environment; in this case by the symmetry of the $Mn^{4+}O_6$ octahedra. As the content of Bi increases the Mn–O are more distorted, providing a lower-symmetry environment for Mn^{4+}. Although it is not well understood, it is observed that the anisotropy of the environment (either shape anisotropy [31] or coordination anisotropy) tends to favor an in-plane configuration of the magnetic moments. The present example nicely illustrates this trend.

In all the samples the magnetic interactions between the two Mn^{3+} cations inside the pyramidal dimers are antiferromagnetic and the magnetic moments are oriented in the ab plane in such a way that the moment direction is nearly 'perpendicular' to the base of the pyramid. The path for the superexchange interaction between the Mn^{3+} ions of the dimer is Mn^{3+}–O1–Mn^{3+}, with a bonding angle around 98°–99° and distances decreasing from 2.95(1) Å for $x = 0.2$ to 2.913(6) Å for $x = 0.8$.

This magnetic coupling between the Mn^{3+} inside the dimers could be responsible for the residual magnetization found below 200–300 K. Taking into account the expected electronic configuration for Mn^{4+} and Mn^{3+} ions (t_{2g}^3 and $t_{2g}^3e_g^1$ respectively) the superexchange interaction across Mn^{4+}–O2–Mn^{4+} paths (along the chains) takes place via t_{2g}–t_{2g} orbitals, whereas for Mn^{3+}–O3–Mn^{3+} (within the dimers) it takes place via e_{2g}–e_{2g} orbitals. Thus, given the directionality of the d orbitals, the e_{2g}–e_{2g} superexchange interaction is, in general, stronger than that observed via t_{2g}–t_{2g} orbitals; this fact suggests that the coupling between Mn^{3+} moments within the dimers is stronger and would take place at higher temperatures, up to 200–300 K [11]. The long-range order established below T_N is a result of the superexchange interactions between the Mn^{4+} ions (along the chains) and Mn^{3+} moments. The values of the magnetic moments obtained at low temperatures for all the samples are significantly lower than those expected for the oxidation states Mn^{4+} (electronic configuration $t_{2g}^3(S = 3/2)$, with a moment of 3 μ_B) and Mn^{3+} (electronic configuration $t_{2g}^3e_g^1(S = 2)$, with an expected moment of 4 μ_B). This reduction could be due to covalency effects.

It is also worth mentioning that $La_{0.8}Bi_{0.2}Mn_2O_5$ and $La_{0.6}Bi_{0.4}Mn_2O_5$ present an anomaly in the thermal variation of a and c lattice parameters around the ordering temperature $T_N = 25$ K. In particular, the a parameter presents a dramatic contraction as temperature increases (figures 12(a) and (b)). This effect was also reported for $LaMn_2O_5$ [11]. This anomaly is related to the magnetic transition, and it occurs probably due to a large degree of spin–lattice coupling, since above T_N the expected thermal expansion of the unit cell is observed. This effect is a symptom of magnetic frustration upon the establishment of the ordered magnetic structure. The present magnetic structures intrinsically involve a high degree of frustration, since along the chains of $Mn^{4+}O_6$ octahedra each Mn1 moment is antiferromagnetically coupled to one neighboring Mn1 spin and ferrimagnetically coupled to one neighboring Mn1 spin in the opposite direction. Conversely, for the Bi-rich compositions, the magnetic coupling of Mn1

spins along the chains is AFM in both directions, thus the magnetostrictive effect is not observed (figures 12(c) and (d)).

Finally, an interesting issue is whether or not we should expect some multiferroic properties in $La_{1-x}Bi_xMnO_5$. The comparison with the paradigmatic example of $TbMn_2O_5$ is enlightening. In this system a complete reversal of electric polarization is induced under external magnetic fields [32]. $TbMn_2O_5$ crystallizes into the space group *Pbam* at RT, as observed in $La_{1-x}Bi_xMnO_5$. At low temperature the manganese sublattice is found to exist in incommensurate and commensurate magnetic phases, in which for both cases the manganese ion moments align in the *ab* plane, forming two spin-density waves with wavevector $\mathbf{k} = (k_x, 0, k_z)$, relieving an otherwise geometrically frustrated system [6, 7]. Along the *c* axis these moments alternate with ferromagnetic and antiferromagnetic layers [7]. Slightly below $T_N = 43$ K, at $T_{FE} = 38$ K, the onset of ferroelectric order with the polarization parallel to the *b* axis is observed. The symmetry of the system in this ferroelectric phase is reduced, probably to space group $Pb2_1m$ [7]. In the present $La_{1-x}Bi_xMnO_5$ compounds, the low resolution and angular range of the available temperature-dependent NPD data do not allow one to reject a plausible phase transition to a polar space group. The possible multiferroicity of the present compounds remains an open question.

5. Conclusions

$La_{1-x}Bi_xMn_2O_5$ oxides present an orthorhombic structure isotypic with RMn_2O_5 oxides. In contrast with RMn_2O_5 (R = rare earths), which present incommensurate magnetic structures, $La_{1-x}Bi_xMn_2O_5$ oxides exhibit commensurate magnetic structures with propagation vectors evolving from $\mathbf{k}_1 = (0, 0, 1/2)$ to $\mathbf{k}_2 = (1/2, 0, 1/2)$ as the Bi content increases, progressively switching from the magnetic structure of $LaMn_2O_5$ to the magnetic structure of $BiMn_2O_5$. These compounds contain two different magnetic cations: Mn^{4+} and Mn^{3+} in different crystallographic environments. While Mn^{3+} magnetic moments lie within the *ab* plane in all the series, Mn^{4+} magnetic moments are directed along the *c* direction for the La-rich compounds and lie within the *ab* plane when the Bi content increases. The changes of the crystallographic and magnetic structures as well as the magnetic properties with Bi content are related to the electronic lone pair of Bi^{3+}, driving significant changes in some bond distances and angles, and thus motivating a change in the balance of the superexchange interactions.

Acknowledgments

We are grateful for financial support from the Spanish Ministry of Science and Technology to project MAT2010-16404 and from the Spanish Ministry of Education and the Fulbright Commission for the grant to M Retuerto. We thank the Laboratoire Léon Brillouin for making all facilities available.

References

[1] Eerenstein W, Mathur N D and Scot J F 2006 *Nature* **442** 759
[2] Cheong S-W and Mostovoy M 2007 *Nature Mater.* **6** 13
[3] Wang C, Guo G-C and He L 2007 *Phys. Rev. Lett.* **99** 177202
[4] Alonso J A, Casais M T, Martínez-Lope M J and Rasines I 1997 *J. Solid State Chem.* **129** 105
[5] Alonso J A, Casais M T, Martínez-Lope M J, Martínez J L and Fernández-Díaz M T 1997 *J. Phys.: Condens. Matter* **9** 8515
[6] Chapon L C, Blake G R, Gutmann M J, Park S, Hur N, Radaelli P G and Cheong S-W 2004 *Phys. Rev. Lett.* **93** 177402
[7] Blake G R, Chapon L C, Radaelli P G, Park S, Hur N, Cheong S-W and Rodríguez-Carvajal J 2005 *Phys. Rev.* B **71** 214402
[8] Kobayashi S, Osawa T, Kimura H, Noda Y, Kagomiya I and Khon K 2004 *J. Phys. Soc. Japan* **73** 1031
[9] Kobayashi S, Osawa T, Kimura H, Noda Y, Kagomiya I and Khon K 2004 *J. Phys. Soc. Japan* **73** 1593
[10] Chapon L C, Radaelli P G, Blake G R, Park S and Cheong S-W 2006 *Phys. Rev. Lett.* **96** 097601
[11] Muñoz A, Alonso J A, Casais M T, Martínez-Lope M J, Martínez J L and Fernández-Díaz M T 2005 *Eur. J. Inorg. Chem.* **4** 685
[12] Bertaut E F, Buisson G, Quezel-Ambrunaz S and Quezel G 1967 *Solid State Commun.* **5** 25
[13] Muñoz A, Alonso J A, Casais M T, Martínez-Lope M J, Martínez J L and Fernández-Díaz M T 2002 *Phys. Rev.* B **65** 144423
[14] Vecchini C, Chapon L C, Brown P J, Chatterji T, Park S, Cheong S-W and Radaelli P G 2008 *Phys. Rev.* B **77** 134434
[15] Buisson G 1973 *Phys. Status Solidi* a **16** 533
[16] Buisson G 1973 *Phys. Status Solidi* a **17** 191
[17] Polyakov V, Plakhty V, Bonnet M, Burlet P, Regnault L-P, Gavrilov S, Zobkalo I and Smirnov O 2001 *Physica* B **297** 208
[18] Wilkinson C, Sinclair F, Gardner P, Forsyth J B and Wanklyn B M R 1981 *J. Phys. C: Solid State Phys.* **14** 1671
[19] Rietveld H M 1969 *J. Appl. Crystallogr.* **2** 65
[20] Rodríguez-Carvajal J 1993 *Physica* B **192** 55
[21] Boucher B, Buhl R and Perrin M 1971 *J. Appl. Phys.* **42** 1615
[22] Jensen G B and Nielsen O V 1974 *J. Phys. C: Solid State Phys.* **7** 409
[23] Muñoz A, Alonso J A, Martínez-Lope M J and Martínez J L 2004 *Chem. Mater.* **16** 4087
[24] Shannon R D 1976 *Acta Crystallogr.* A **32** 751
[25] Retuerto M, Martínez-Lope M J, Krezhov K, Fernández-Díaz M T and Alonso J A 2011 *J. Solid State Chem.* **184** 2428
[26] Larrégola S A, Alonso J A, Pedregosa J C, Martinez-Lope M J, Alguero M, De la Pena-O'shea V, Porcher F and Illas F 2009 *Dalton Trans.* **28** 5453
[27] Larrégola S A, Alonso J A, Sheptyakov D, Alguero M, Muñoz A, Pomjakushin V and Pedregosa J C 2010 *J. Am. Chem. Soc.* **132** 14470
[28] Muñoz A, Alonso J A, Martínez-Lope M J, Falcón H, García-Henández M and Morán E 2006 *Dalton Trans.* **41** 4936
[29] Martinez-Lope M J, Retuerto M, Alonso J A, Sanchez-Benitez J and Fernandez-Diaz M T 2011 *Dalton Trans.* **40** 4599
[30] Goodenough J B 1955 *Phys. Rev.* B **100** 564
[31] Galanakis I, Alouani M and Dreyssé H 2000 *Phys. Rev.* B **62** 3923
[32] Hur N, Park S, Sharma P A, Ahn J S, Guha S and Cheong S-W 2004 *Nature* **429** 392